LEARNING PHASE-SPACE FLOWS USING TIME-DISCRETE IMPLICIT RUNGE-KUTTA PINNS

Álvaro Fernández Corral*^{1,2}, Nicolás Mendoza¹, Armin Iske³, Andrey Yachmenev^{1,4}, and Jochen Küpper^{1,2,4}
¹Center for Free-Electron Laser Science CFEL, Deutsches Elektronen-Synchrotron DESY, Notkestraße 85, 22607

Hamburg, Germany

²Department of Physics, Universität Hamburg, Luruper Chaussee 149, 22761 Hamburg, Germany
 ³Department of Mathematics, Universität Hamburg, Bundesstraße 55, 20146 Hamburg, Germany
 ⁴Center for Ultrafast Imaging, Universität Hamburg, Luruper Chaussee 149, 22761 Hamburg, Germany

2024-09-26

ABSTRACT

We present a computational framework for obtaining multidimensional phase-space solutions of systems of non-linear coupled differential equations, using high-order implicit Runge-Kutta Physics-Informed Neural Networks (IRK-PINNs) schemes. Building upon foundational work originally solving differential equations for fields depending on coordinates [*J. Comput. Phys.* **378**, 686 (2019)], we adapt the scheme to a context where the coordinates are treated as functions. This modification enables us to efficiently solve equations of motion for a particle in an external field. Our scheme is particularly useful for explicitly time-independent and periodic fields. We apply this approach to successfully solve the equations of motion for a mass particle placed in a central force field and a charged particle in a periodic electric field.

Keywords physics-informed neural networks · implicit Runge-Kutta methods · phase-space flows

1 Introduction

Physics-Informed Neural Networks (PINNs) have emerged as a prominent and dynamic area of research for solving differential equations [1, 2], for example, for modeling the physics of fluid dynamics [3–5] or quantum mechanics [6]. Unlike traditional neural networks, that learn solely from data, PINNs use both data and physical equations to guide the learning process [7–9].

PINNs can be effectively employed using continuous and discrete representations of time. The time-continuous approach uses space and time variables as inputs, and learn to satisfy the differential equations across the entire domain of interest. This can be impractical without data distributed across multiple time slices. In addition, time-continuous PINNs also encounter difficulties with high-frequency oscillations and stiff problems, lacking a clear strategy to deal with them. On the other hand, the discrete-time PINNs learn to model changes within a fixed discrete time step, utilizing only spatial information from a single time slice. This approach improves the accuracy in solving stiff problems [10] by leveraging the *A*-stability of implicit Runge-Kutta (IRK) methods [11]. This is especially significant for tackling the stiff problems prevalent in particle trajectory simulations and Differential Algebraic Equations (DAEs), known for their inherent infinite stiffness [11, 12].

In this paper, we extend the discrete-time IRK-PINN scheme [1] by generalizing it to a larger number of dimensions in both input variables and output quantities. Importantly, we have adapted this approach to develop a new efficient numerical scheme tailored to finding phase-space flows of classical particle trajectories, described by second-order differential equations of motions. The new algorithm enables the simultaneous learning of all possible trajectories within the specified phase-space and is particularly suited for explicitly time-independent and time-periodic forces.

^{*}Corresponding author: alvaro.fernandez@cfel.de

The manuscript is organized as follows: The details and application of the IRK-PINN scheme to phase-space flows are described in Section 2. Section 3 presents some illustrative application examples with time-independent and periodic forces. The review and application details of the IRK-PINN scheme, including its successful application to a number of various differential equations, are elaborated in Appendix A–C.

2 Phase-space flows with IRK-PINNs

In applications to physics problems, the IRK-PINN method was primarily applied to functions $\mathbf{u}: \mathbb{R}^{1+d} \to \mathbb{R}^m$ which represent background "fields" of the system, such as the temperature, pressure, velocity flow, heat convection, etc., see Appendix A for details. The literature on applying PINN-based IRK schemes to particle trajectory analysis in physical systems is limited, with the exception of work focusing on first-order differential equations [13]. We are interested in solving differential equations of the general form

$$\mathbf{F}(\mathbf{x}, \dot{\mathbf{x}}, \ddot{\mathbf{x}}, \dots, t) = \mathbf{0},\tag{1}$$

which encompass, for example, Newton's equation, expressed as $\ddot{\mathbf{x}} = \mathbf{f}(\mathbf{x}, \dot{\mathbf{x}}, t)$. Our goal is to adapt and apply the IRK-PINNs scheme to effectively compute particle flows $\mathbf{x}(t)$ resulting from a force $\mathbf{f}(\mathbf{x}, \dot{\mathbf{x}}, t)$. We begin by transforming the second-order Newton-type differential equation into a system of first-order differential equations using the 2d-dimensional phase-space coordinates, denoted as $\chi = (\mathbf{x}, \dot{\mathbf{x}})$, with the dimensionality d of the vector \mathbf{x} . We define our function of interest as $\mathbf{u}(t,\chi_i) = \hat{\chi}_i(t)$, with $\hat{\chi}_i : \mathbb{R} \to \mathbb{R}^{2d}$ representing the flow function. This flow function defines the trajectory of any point in phase-space – a one parameter curve in our phase-space manifold – that satisfies the condition $\hat{\chi}_i(t_n) = \chi_i$. By adhering to the equations of motions, this condition ensures a unique solution. Indeed, since the value of $\mathbf{u}(t_n,\chi_i)$ at the initial time t_n is $\mathbf{u}_n(\chi_i) = \chi_i$, we can determine the phase-space values at time t_{n+1} by employing the IRK-PINNs time propagation method. By applying the IRK scheme, see (5) in Appendix A, using a fully connected feedforward neural network (FNN) also known as a multilayer perceptron (MLP), to the general trajectory equation (1), we thus determine the trajectories that satisfy the following set of differential equations

$$0 = \mathcal{N}[\chi] + \frac{d}{dt}\chi \equiv \begin{pmatrix} \dot{\mathbf{x}} \\ \mathbf{f}(\mathbf{x}, \dot{\mathbf{x}}, t) \end{pmatrix} + \frac{d}{dt} \begin{pmatrix} \mathbf{x} \\ \dot{\mathbf{x}} \end{pmatrix}.$$
 (2)

Any additional boundary conditions that may be essential for the well-defined nature of the problem can also be accommodated.

The algorithm's strength lies in its ability to predict the future state of every point in the phase-space at time t_{n+1} by learning from only a limited sample of phase-space data at the initial time t_n . In addition, as a high-order IRK algorithm, it is well suited to solve stiff problems, enhancing computational efficiency in the propagation of numerous trajectories.

Moreover, this algorithm is particularly effective for forces that are explicitly time-independent and/or periodic in time. If the force doesn't explicitly change over time and only relies on the position or velocity of the particle, both being implicitly time-dependent vector fields, the neural network can effectively predict the trajectories by learning from a training set in the phase-space. For periodic forces, we impose the time-propagation step size to match the period of the force $\Delta t := T$, so that the neural network output $\chi(t_{n+1})$ would reside on a phase-space manifold identical to the initial one at t_n . The periodic nature of the force is essential, as the phase-space manifold is entirely dependent on the force governing the particles' motions, necessitating that $\mathbf{f}(\mathbf{x},t_n+\Delta t)$ remains equivalent to $\mathbf{f}(\mathbf{x},t_n)$. In both cases, or a combination, the phase-space manifold remains unchanged after a single time step propagation. Consequently, to predict trajectories for subsequent time slices, the IRK-PINN algorithm can be recurrently applied after training.

3 Results

3.1 Keplerian orbits

A massive body under the action of a central potential moves according to Newton's equation of gravity. The trajectories that orbiting objects follow are called Keplerian orbits. The analytical solution of N-body problems is complicated due to the implicit time-dependency of the force $F \sim 1/r_{ij}^2(t)$, arising from the varying distances between different objects $r_{ij}^2(t)$. For this reason, low-order IRK schemes with small time stepping were used to propagate these systems [14]. Following the discussion in the previous section, our phase-space flows approach offers an efficient alternative for propagating these explicitly time-independent systems. This is achieved by recurrently applying the neural network, requiring only a single training session of the IRK-PINN and thus eliminating the need for additional approximations.

We focus on central forces, which conserve angular momentum, leading to the confinement of trajectories within a two-dimensional plane defined by the initial momentum and the radial vector [15]. Initially, our efforts were directed at

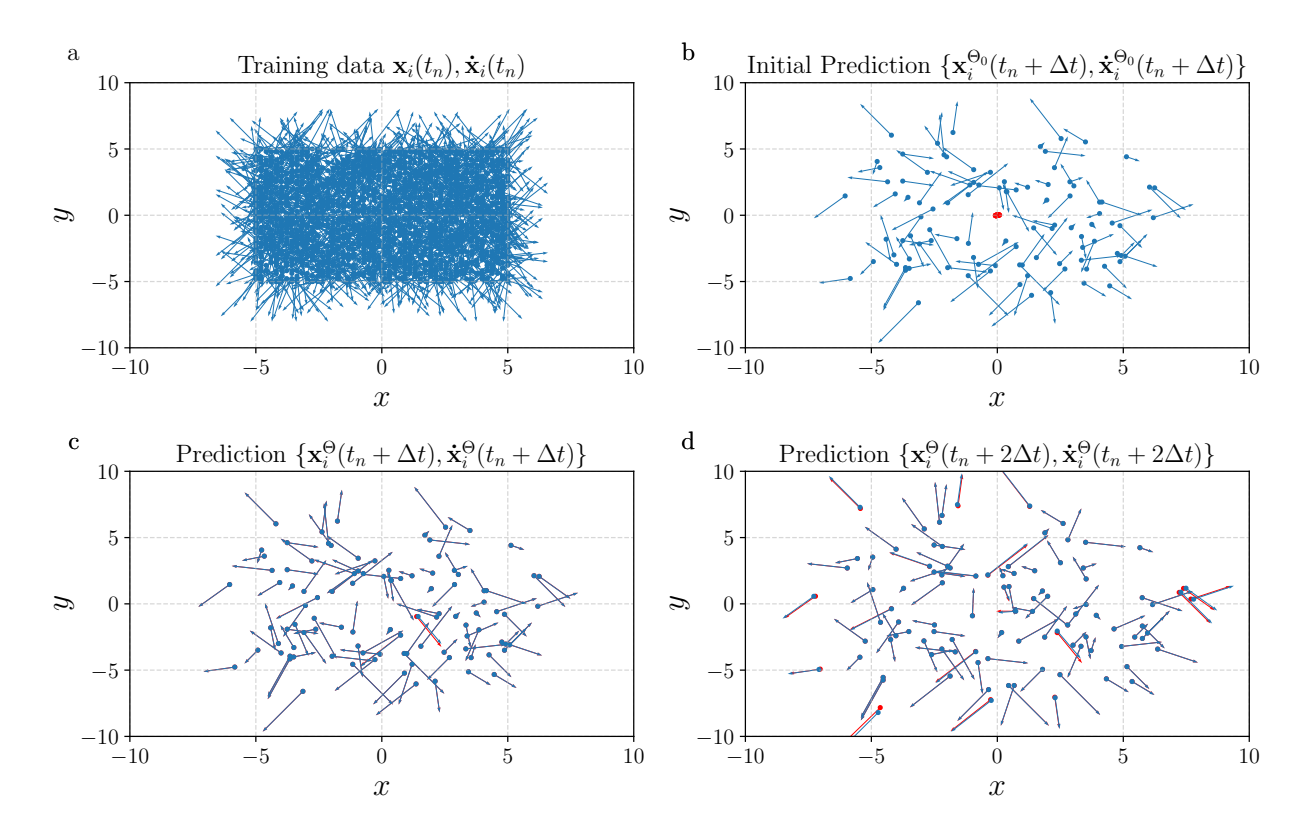


Figure 1: Calculated trajectories of a particle in a central Gaussian potential, with potential depth $V_0=10$ and extension $a=\sqrt{5}$. The IRK-PINN and numerically exact solutions are plotted with blue and red colours, respectively. Panel (a) shows the entire training phase space consisting of 2 000 points. Due to the complex distribution of the solutions with respect to the initial position, a big set of training data is needed. Panel (b) shows the result of the low-order IRK method (blue) on the validation set, consisting of 100 points, for visual clarity. In addition, the PINN guess on parameter initialisation is displayed (red). Panels (c) and (d) show the IRK-PINN predictions on the validation set for the time step Δt and $2\Delta t$, respectively. The IRK-PINNs approach adopted a Runge-Kutta order q=100, time step $\Delta t=0.8$, dense MLP containing 5 hidden layers with 200 nodes each, and a bipolar sigmoid as the activation function. The training was carried out for $100\,000$ epochs with the ADAM optimiser followed by $40\,000$ epochs with L-BFGS-B. Total L^1 -error $=0.58\,\%$.

solving the fixed-central-mass problem in a two-dimensional Euclidian space with a Coulomb potential. However, after experimenting with various MLPs and parameters, we observed that the algorithm was unable to accurately predict the trajectories for this problem. We believe that this limitation arises from the fact that not all points in the initial phase-space correspond to physically viable solutions. Given that the algorithm attempts to simultaneously solve for all trajectories, these divergent paths likely cause a general diverging behaviour of the method.

The accurate and efficient calculation of Keplerian orbits is critical in simulations of particle diffraction from the Coulomb potential with a small impact parameter. This is especially important for simulations of laser-induced electron diffraction [16], where the diffraction of highest-energy electrons is influenced by these orbital dynamics [17–19].

To avoid singularities, we replaced the Coulomb potential with a central potential characterized by a Gaussian function $V(\mathbf{x}) = -V_0 \exp(-\mathbf{x}^2/a^2)$, where V_0 is the depth of the potential well and the a parameter determines its extent. This choice of potential is a standard first-order approximation to the Coulomb potential in strong-field physics [20] and provides Kepler-like orbits, while not provoking diverging trajectories, due to its finite value at the origin. Defining the force as the negative gradient of this potential, the equations of motion become

$$\mathcal{N}[\chi] = -\begin{pmatrix} \dot{\mathbf{x}} \\ -\nabla_{\mathbf{x}} V(\mathbf{x}) \end{pmatrix} \equiv -\begin{pmatrix} \dot{\mathbf{x}} \\ -2\frac{V_0}{a^2} \exp(-\frac{\mathbf{x}^2}{a^2}) \mathbf{x} \end{pmatrix}. \tag{3}$$

The domain of the model is $(\mathbf{x}, \dot{\mathbf{x}}) \in \Omega = \mathbb{R}^2 \times \mathbb{R}^2$. Considering that the phase-space flows approach uses an equal number of phase-space coordinates and objective functions, we will work within a 4-dimensional phase-space and

output space. For benchmarking the IRK-PINN results, we generated accurate solutions using low-order adaptive IRK schemes, specifically Kværnø's 5/4 method [21], as implemented in the Diffrax library [22].

The accuracy of the IRK-PINNs solution, along with the details of the neural network, are demonstrated in FIG. 1. It is important to note that the central force in this model is explicitly time-independent. This aspect, combined with comprehensive solution for the entire phase space, enables us to propagate in time steps of Δt by recurrently applying the model at each time step. To illustrate this, in FIG. 1 d we show the accuracy of predictions of the neural network at a doubled time step $2\Delta t$. In addition, this panel shows the ability of the PINN to predict trajectories from points that are not contained inside the training region.

3.2 Charged particle under the action of a sinusoidal laser

In this example, we consider the motion of a charged particle under the influence of a periodic external electric field, i. e., a laser field. The force exerted on a particle with charge q by an external field $\mathbf{E}(\mathbf{x},t)$ is given by $\mathbf{F}(\mathbf{x},t)=q\mathbf{E}(\mathbf{x},t)$. As in the previous example, we continue to work within a 4-dimensional phase space defined by $(\mathbf{x},\dot{\mathbf{x}})\in\Omega=\mathbb{R}^2\times\mathbb{R}^2$, also corresponding to a 4-dimensional output space.

For simplicity, we assume that the wavelength of the laser field is much larger than the scale of particle movement. The electric field, characterised by an angular frequency ω and incident at an angle α relative to the x-axis, is represented by the function $\mathbf{E}(\mathbf{x},t)=(E_x(t),E_y(t))=(A\cos(\omega t)\cos(\alpha),A\cos(\omega t)\sin(\alpha)),$ where A denotes field's amplitude. Choosing the unit system M=q=1, the differential equation of motion can be expressed as

$$\mathcal{N}[\chi] = -\begin{pmatrix} \dot{\mathbf{x}} \\ \mathbf{E}(\mathbf{x}) \end{pmatrix} = -\begin{pmatrix} \dot{x} \\ \dot{y} \\ A\cos(\omega t)\cos(\alpha) \\ A\cos(\omega t)\sin(\alpha) \end{pmatrix}. \quad (4)$$

This particular form of the laser field is chosen for its analytical solvability, substantive complexity, and periodic behaviour in time. Given any initial conditions $(x_0, y_0, \dot{x_0}, \dot{y_0})$ at time t_0 , the analytical solution can be readily obtained. We examine the system with a laser of period $T=1:=\Delta t$, amplitude A=10 and incident angle $\alpha = 0.5$. To benchmark our IRK-PINNs implementation, we compare its results for different Runge-Kutta orders with the analytical solution. The results of the simulations and the details of the neural networks used are presented in FIG. 2. These results were obtained for multiple periods of the electric field by recurrently applying the neural network, which was trained only once, for the first period, using a set of training points distributed across a subset of the phase-space. For the purpose of illustration and avoiding overfitting, a validation set contained in a different subset of the phase-space was used to generate the plots.

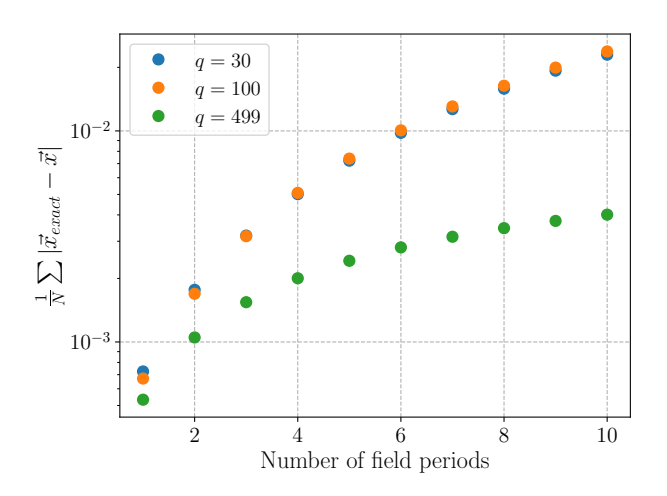


Figure 2: Accuracy of IRK-PINNs method for different Runge-Kutta orders q=30,100,499 in solving the trajectories of a charged particle in periodic electric field, as described by (4) with the parameters $\alpha=0.5$ and A=10. Accuracy is quantified using the L^1 -error calculated on a validation set of 2 500 points. Training involved 50 000 epochs each with the ADAM and L-FBGS-B optimizers. The model architecture included an MLP with 5 hidden layers, each composing 32 nodes, and employed the SiLU(x) activation function. The training utilized 5 000 points.

4 Conclusions

We introduced a versatile algorithm designed to effectively solve a broad range of differential equations. The algorithm was validated by generating accurate results for both functional PDEs and equations of motion. Notably, the application of PINNs as a propagator for explicitly time-independent and periodic forces represents a significant advancement over conventional low-order IRK methods.

Further work should focus on addressing the problem of divergent trajectories, particularly in cases like Keplerian orbits under a Coulomb $\sim 1/|\mathbf{x}|$ potential. Overcoming this divergences would particularly enhance the algorithm's utility in solving stiff dynamical systems, such as the N-body problem [14] and the dynamics of charged particles in time-independent or periodic external fields [17, 18].

Acknowledgements

This work was supported by Deutsches Elektronen-Synchtrotron DESY, a member of the Helmholtz Association (HGF), including the Maxwell computational resource operated at DESY, by the Data Science in Hamburg HELMHOLTZ Graduate School for the Structure of Matter (DASHH, HIDSS-0002), and by the Deutsche Forschungsgemeinschaft (DFG) through the cluster of excellence "Advanced Imaging of Matter" (AIM, EXC 2056, ID 390715994).

References

- [1] M. Raissi, P. Perdikaris, and G. Karniadakis, J. Comput. Phys. 378, 686 (2019).
- [2] S. Cuomo, V. S. Di Cola, F. Giampaolo, G. Rozza, M. Raissi, and F. Piccialli, J. Sci. Comput. 92, 88 (2022).
- [3] X. Jin, S. Cai, H. Li, and G. E. Karniadakis, J. Comput. Phys. 426, 109951 (2021).
- [4] H. Eivazi, M. Tahani, P. Schlatter, and R. Vinuesa, Phys. Fluids 34, 075117 (2022).
- [5] C. Rao, H. Sun, and Y. Liu, Theor. Appl. Mech. Lett. 10, 207 (2020).
- [6] K. Shah, P. Stiller, N. Hoffmann, and A. Cangi, Physics-informed neural networks as solvers for the time-dependent Schrödinger equation (2022), arXiv:2210.12522 [cs, stat].
- [7] Z. Chen, Y. Liu, and H. Sun, Nat. Commun. 12, 10.1038/s41467-021-26434-1 (2021).
- [8] H. Xu, D. Zhang, and N. Wang, J. Comput. Phys. 445, 110592 (2021).
- [9] H. Xu and D. Zhang, Phys. Rev. Research 3, 033270 (2021).
- [10] P. Sharma, L. Evans, M. Tindall, and P. Nithiarasu, Arch. Comput. Methods Eng. 30, 2929 (2023).
- [11] E. Hairer and G. Wanner, Solving Ordinary Differential Equations II. Stiff and Differential-Algebraic Problems, Vol. 14 (Springer Berlin, Heidelberg, 1996).
- [12] S. Kim, W. Ji, S. Deng, Y. Ma, and C. Rackauckas, Chaos 31, 093122 (2021).
- [13] C. Moya and G. Lin, Neural. Comput. Appl. 35, 3789 (2022).
- [14] M. Antoñana, E. Alberdi, J. Makazaga, and A. Murua, Celestial Mech. & Dyn. Astron. 134, 10.1007/s10569-022-10081-9 (2022).
- [15] H. Goldstein, Classical mechanics (Pearson Education, Amsterdam, 2002).
- [16] C. I. Blaga, J. Xu, A. D. DiChiara, E. Sistrunk, K. Zhang, P. Agostini, T. A. Miller, L. F. DiMauro, and C. D. Lin, Nature 483, 194 (2012).
- [17] N. I. Shvetsov-Shilovski, Eur. Phys. J. D 75, 130 (2021).
- [18] J. Wiese, J. Onvlee, S. Trippel, and J. Küpper, Phys. Rev. Research 3, 013089 (2020), arXiv:2003.02116 [physics]
- [19] J. Wiese, *Strong-field photoelectron imaging of complex molecules*, Dissertation, Universität Hamburg, Hamburg, Germany (2020).
- [20] J. Toulouse, A. Savin, and H.-J. Flad, Int. J. Quantum Chem. 100, 1047 (2004), https://onlinelibrary.wiley.com/doi/pdf/10.1002/qua.20259.
- [21] A. Kværnø, BIT Numer. Math. 44, 489 (2004).
- [22] P. Kidger, On Neural Differential Equations, Dissertation, University of Oxford (2021).
- [23] A. Iserles, A First Course in the Numerical Analysis of Differential Equations, 2nd ed. (Cambridge University Press, 2008).
- [24] S. González Pinto, S. Pérez Rodríguez, and J. Montijano Torcal, J. Comput. & Appl. Math. 82, 129 (1997), 7th ICCAM 96 Congress.
- [25] E. Hairer and G. Wanner, J. Comput. & Appl. Math. 111, 93 (1999).
- [26] C. A. Kennedy and M. H. Carpenter, Appl. Num. Math. 146, 221 (2019).
- [27] J. Bradbury, R. Frostig, P. Hawkins, M. J. Johnson, C. Leary, D. Maclaurin, G. Necula, A. Paszke, J. VanderPlas, S. Wanderman-Milne, and Q. Zhang, JAX: composable transformations of Python+NumPy programs (2018).
- [28] J. Heek, A. Levskaya, A. Oliver, M. Ritter, B. Rondepierre, A. Steiner, and M. van Zee, Flax: A neural network library and ecosystem for JAX (2023).

- [29] DeepMind, I. Babuschkin, K. Baumli, A. Bell, S. Bhupatiraju, J. Bruce, P. Buchlovsky, D. Budden, T. Cai, A. Clark, I. Danihelka, A. Dedieu, C. Fantacci, J. Godwin, C. Jones, R. Hemsley, T. Hennigan, M. Hessel, S. Hou, S. Kapturowski, T. Keck, I. Kemaev, M. King, M. Kunesch, L. Martens, H. Merzic, V. Mikulik, T. Norman, G. Papamakarios, J. Quan, R. Ring, F. Ruiz, A. Sanchez, L. Sartran, R. Schneider, E. Sezener, S. Srinivasan, M. Stanojević, W. Stokowiec, L. Wang, G. Zhou, and F. Viola, The DeepMind JAX Ecosystem (2020).
- [30] D. P. Kingma and J. Ba, arXiv preprint arXiv:1412.6980 (2015).
- [31] R. H. Byrd, P. Lu, J. Nocedal, and C. Zhu, SIAM J. Sci. Comp. 16, 1190 (1995).
- [32] M. Blondel, Q. Berthet, M. Cuturi, R. Frostig, S. Hoyer, F. Llinares-López, F. Pedregosa, and J.-P. Vert, in *Advances in Neural Information Processing Systems (NIPS)*, Vol. 35 (Curran Associates, Inc., 2022) pp. 5230–5242, arXiv:2105.15183 [cs].
- [33] M. Panicker and C. Babu, IOSR J. Eng. 02, 1352 (2012).
- [34] R. C. Daileda, The two dimensional heat equation (2012).
- [35] G. I. Taylor and A. E. Green, Proc. Royal Soc. London A 158, 499 (1937).

A High-order implicit Runge-Kutta scheme

We start by examining a vector-valued function $\mathbf{u}: \Sigma \to \mathbb{R}^m$, which is defined over spacetime vectors $(t, \mathbf{x}) \in \Sigma := \mathbb{R} \times \Omega \subset \mathbb{R}^{1+d}$ in the domain formed by a combination of 1-dimensional time and d-dimensional space. This function is defined to be the solution of a set of non-linear coupled differential equations, represented as $\partial_t \mathbf{u} + \mathcal{N}[\mathbf{u}] = 0$, $\forall (t, \mathbf{x})$ in Ω . Additionally, we considered the possibility of incorporating boundary conditions, denoted as $\mathcal{B}_{\alpha}[\mathbf{u}(\partial\Omega)] = 0$, which could depend on the derivatives of \mathbf{u} at the boundary.

We sought to develop an algorithm that utilizes the dataset $\{\mathbf{x}_k, \mathbf{u}(t_n, \mathbf{x}_k)\}_{k=1}^N$ at a specific time slice t_n and the differential equations representing the time evolution to accurately predict $\mathbf{u}(t_{n+1}, \mathbf{x})$ at the next time slice t_{n+1} . To describe the time propagation from t_n to t_{n+1} , we introduced an IRK scheme of q-th order, defined by a set of coupled equations

$$\mathbf{u}_{n+c_i} = \mathbf{u}_n - \Delta t \sum_{j=1}^q a_{ij} \mathcal{N}[\mathbf{u}_{n+c_j}] \quad \forall i \in \{1, \dots, q\},$$
 (5a)

$$\mathbf{u}_{n+1} = \mathbf{u}_n - \Delta t \sum_{j=1}^q b_j \mathcal{N}[\mathbf{u}_{n+c_j}], \tag{5b}$$

where $\mathbf{u}_{n+c_i}(\mathbf{x}) \coloneqq \mathbf{u}(t_n + c_i \Delta t, \mathbf{x})$, $\Delta t = t_{n+1} - t_n$ and a_{ij} , b_j , and c_i are the Butcher-tableau coefficients for a chosen IRK order q. The computation of the Butcher tableau involves expanding the solution into a Taylor series and matching the coefficients to the actual solution up to the desired order of accuracy. The choice of this coefficients is not unique, and it specifies the particular IRK method. We chose the Gauss-Legendre Runge-Kutta method, which is A-stable for all orders [23], to find the coefficients throughout our implementation. However, other methods, such as the Lobatto [24], the Radau [25], or the diagonally implicit Runge-Kutta methods [26], result in different accuracy, stability, and efficiency properties. Testing the pros and cons of using different Butcher-tableau coefficients in applications with IRK-PINNs is beyond the scope of this manuscript, although it should be further explored in the future.

The theoretical analysis of the IRK algorithm suggests that the deviation from the exact result scales as $\mathcal{O}(\Delta t^{2q})$ [23]. Although it may initially appear that the error would grow with increasing q for time steps $\Delta t > 1$, it is important to recognize that this error is dimensionful and requires a constant to render it dimensionless for proper interpretation.

For a chosen IRK order q, we place a neural network prior on all intermediate calculations and the final output

$$\mathcal{U} := (\mathbf{u}_{n+c_1}, \dots, \mathbf{u}_{n+c_n}, \mathbf{u}_{n+1}). \tag{6}$$

We observe that $\mathcal{U}(\mathbf{x}) \in \mathbb{R}^{m \times (q+1)}$ can be conceptualized as an $m \times (q+1)$ matrix, where m is the output dimension of \mathbf{u} which is not necessarily equal 1. Consequently, we employ an MLP denoted by $\mathcal{U}^{\theta}: \mathbb{R}^{d} \to \mathbb{R}^{m \times (q+1)}$, to closely approximate the desired function \mathcal{U} . We define \mathbf{u}_{j}^{θ} in a manner analogous to (6) as the parameter-dependent approximation. Subsequently, we define a set of parameter-dependent quantities to be used in the loss function as

$$\mathbf{k}_{i}^{\theta} = \mathbf{u}_{n+c_{i}}^{\theta} + \Delta t \sum_{j=1}^{q} a_{ij} \mathcal{N}[\mathbf{u}_{n+c_{j}}^{\theta}] \quad \forall i \in \{1, \dots, q\}$$
 (7a)

$$\mathbf{k}_{q+1}^{\theta} = \mathbf{u}_{n+1}^{\theta} + \Delta t \sum_{j=1}^{q} b_j \mathcal{N}[\mathbf{u}_{n+c_j}^{\theta}]. \tag{7b}$$

Comparing (7) with (5), it is evident that if \mathcal{U}^{θ} effectively approximates \mathcal{U} , then the earlier definition implies $\mathbf{k}_{i}^{\theta} \approx \mathbf{u}_{n} \ \forall i \in \{1, \dots, q+1\}$. Using this relationship, we can express the loss function as

$$\mathcal{L}_{\mathcal{N}}(\theta, \{\mathbf{x}_k\}_{k=1}^N) = \frac{1}{N} \sum_{k=1}^N \sum_{i=1}^{q+1} \left\| \mathbf{k}_i^{\theta}(\mathbf{x}_k) - \mathbf{u}_n(\mathbf{x}_k) \right\|^2, \tag{8}$$

where $\{\mathbf{x}_k\}_{k=1}^N$ is a set of spatial points randomly distributed in the phase-space Ω .

Furthermore, if the differential equations include A boundary conditions of the type $\mathcal{B}_{\alpha}[\mathbf{u}(\partial\Omega)] = 0$, an additional term can be added to the loss function

$$\mathcal{L}_{\mathcal{B}}(\theta, \{\hat{\mathbf{x}}_b\}_{b=1}^B) = \frac{1}{B} \frac{1}{A} \sum_{b=1}^B \sum_{\alpha=1}^A \left\| \mathcal{B}_{\alpha}[\mathbf{u}(\hat{\mathbf{x}}_b)] \right\|^2, \tag{9}$$

where $\{\hat{\mathbf{x}}_b\}_{b=1}^B$ is a set of spatial points distributed in the boundary $\partial\Omega$.

The total loss function used in the optimization is expressed as a weighted sum of the aforementioned terms, as

$$\mathcal{L}(\theta, \{\mathbf{x}_k\}_{k=1}^N, \{\hat{\mathbf{x}}_b\}_{b=1}^B) = \omega_{\mathcal{N}} \mathcal{L}_{\mathcal{N}} + \omega_{\mathcal{B}} \mathcal{L}_{\mathcal{B}}.$$
(10)

To ensure best convergence, the ratio of the weights ω_N and ω_B can be chosen different depending on the problem.

B Methodology

We implemented the IRK-PINNs using the JAX [27] and Flax [28] Python libraries and optimized the weights of the PINN by initially approaching the minimum using Optax [29] with the Adam first-order optimizer [30] and then refined the result by switching to the second-order optimization L-BFGS-B [31] available in the Jaxopt library [32]. For the PINN, we employed a fully-connected dense MLP with different number and structure of hidden layers and types of activation functions, depending on the problem addressed. We found that $SiLU(x) = \frac{x \exp(x)}{1 + \exp(x)}$ and bipolar sigmoid $f(x) = \frac{\exp(x) - 1}{\exp(x) + 1}$ [33] activation functions work best for the problems considered in this study.

For benchmarking, we obtained accurate results using the low-order Runge-Kutta approach from the Diffrax library [22], which provides various implicit and explicit Runge-Kutta methods of different orders.

Our developed model is highly versatile and easy to use. Using just one class type, it successfully handled a range of applications, some of which are highlighted in Appendix C.

C Additional results

In this section, we present the performance of the IRK-PINNs scheme applied to systems that handle fields $\mathbf{u}:\mathbb{R}^{1+d}\to\mathbb{R}^m$, similar to those investigated previously [1]. These differ conceptually from a particle's equations of motion, which deal with coordinates $(\mathbf{x},\dot{\mathbf{x}}):\mathbb{R}\to\mathbb{R}^{2d}$, in the manner that fields do not have to follow a direct relation with the phase-space of the system.

In the following, we selected a number of functional PDEs with different input/output dimensions to illustrate the versatility of the algorithm.

C.1 Heat Equation in a 2D Plate

We deal with a system with a 2-dimensional input: the heat equation over a surface. This equation describes the evolution of a scalar field $T: \mathbb{R}^{2+1} \to \mathbb{R}$, representing the temperature of a 2D system in time. Using our formalism, the heat equation is given by

$$\mathcal{N}[T] = -c^2 \nabla^2 T,\tag{11}$$

where c is the thermal diffusivity, a constant that measures the rate of heat transfer inside the material.

We will deal with the system shown in [34], which is a two dimensional sheet $(x,y) \in \Omega = [0,2]^2$ with c=1/3 and periodic boundary conditions for the temperature given by T(t,0,y) = T(t,2,y) = T(t,x,0) = T(t,x,2) = 0. We will also impose the initial condition of a heated lower half plane $T(0,x,y) = 50(1-\Theta(y-1))$, with Θ being the unit (Heaviside) step function. In essence, this represents a 2×2 square that is initially heated and in contact with a cold resevoir at its boundary with T=0. The solution to this equation is given by

$$T(t,x,y) = \sum_{m,n=1}^{\infty} \frac{200}{\pi^2} \frac{(1+(-1)^{m+1})(1-\cos\frac{n\pi}{2})}{mn}.$$

$$\cdot \sin\frac{m\pi x}{2} \sin\frac{n\pi y}{2} e^{-\frac{c^2\pi^2}{4}(m^2+n^2)t}.$$
(12)

The results of our IRK-PINN prediction, compared to (12) and the description of the used neural network, are shown in FIG. 3. The IRK-PINN is able to learn the solution of the heat equation, even for relatively small neural network and sample size.

C.2 Incompressible Navier-Stokes equation: Taylor-Green vortices

The Navier-Stokes Equations describe the motion of Newtonian fluids. In these equations, the variation of the quantity of fluid and its velocity are studied, usually in a compact or periodic domain. The pressure, temperature and density

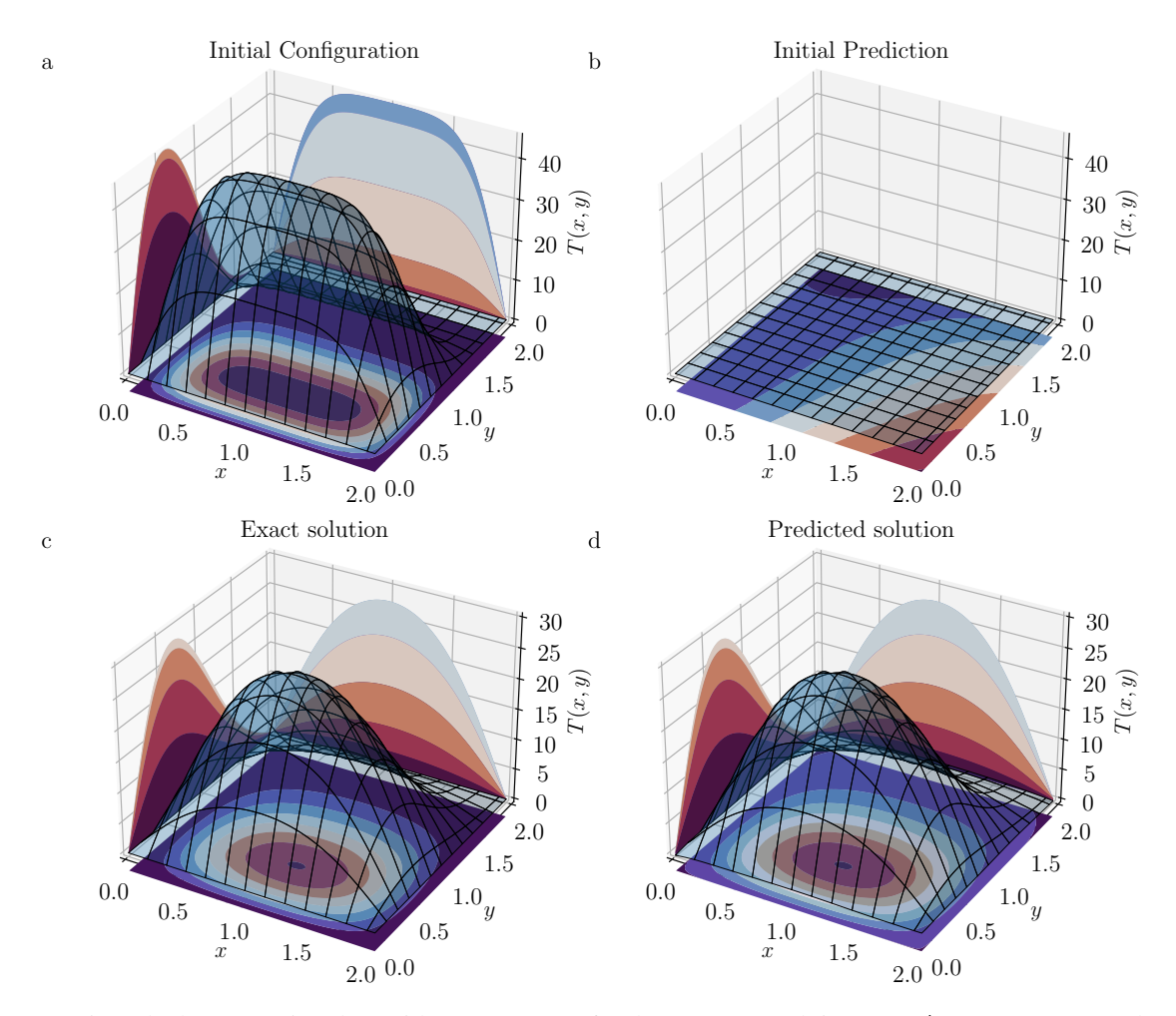


Figure 3: Fit to the heat equation data with IRK-PINNs of order q=100 and time step $\Delta t=0.7$, compared to the analytical solution of the problem. The training was performed for 25000 epochs with ADAM, 40000 epochs with L-BFGS-B, using an MLP with 20 hidden layers with 32 nodes each and SiLU as activation function. (a) The initial configuration space, consisting of N=500 points. (b) The prediction of the PINN on parameter inisialization. This initial prediction is totally arbitrary and far from the correct result, which shows the robustness of the learning process. (c) The analytical solution of the heat equation after one time step. (d) The prediction of the IRK-PINN after training. Total L^1 error =4.81%

of the fluid also play a role in the description, as well as its viscosity. The search for general solutions to this set of equations is still a very active field of research, with analytical solutions being rarely available for specific assumptions. We study the Taylor-Green vortex [35], which is an incompressible Navier-Stokes equation that has an exact closed form in Cartesian coordinates. The Taylor-Green vortex system is described by

$$\mathcal{N}[u] = u\partial_x u + v\partial_y u + \frac{1}{\rho}\partial_x p - \nu(\partial_x^2 u + \partial_y^2 u)$$
(13a)

$$\mathcal{N}[v] = u\partial_x v + v\partial_y v + \frac{1}{\rho}\partial_y p - \nu(\partial_x^2 v + \partial_y^2 v), \tag{13b}$$

where u(t,x,y) and v(t,x,y) are respectively the x and y components of the velocity fields of the fluid, ν is the viscosity, ρ is the mass density, and p(t,x,y) is the pressure of the fluid. To account for the continuity equation for these velocities, which is $\partial_x u + \partial_y v = 0$, we treat it as a boundary condition and add it to our algorithm as an extra term to the loss function.

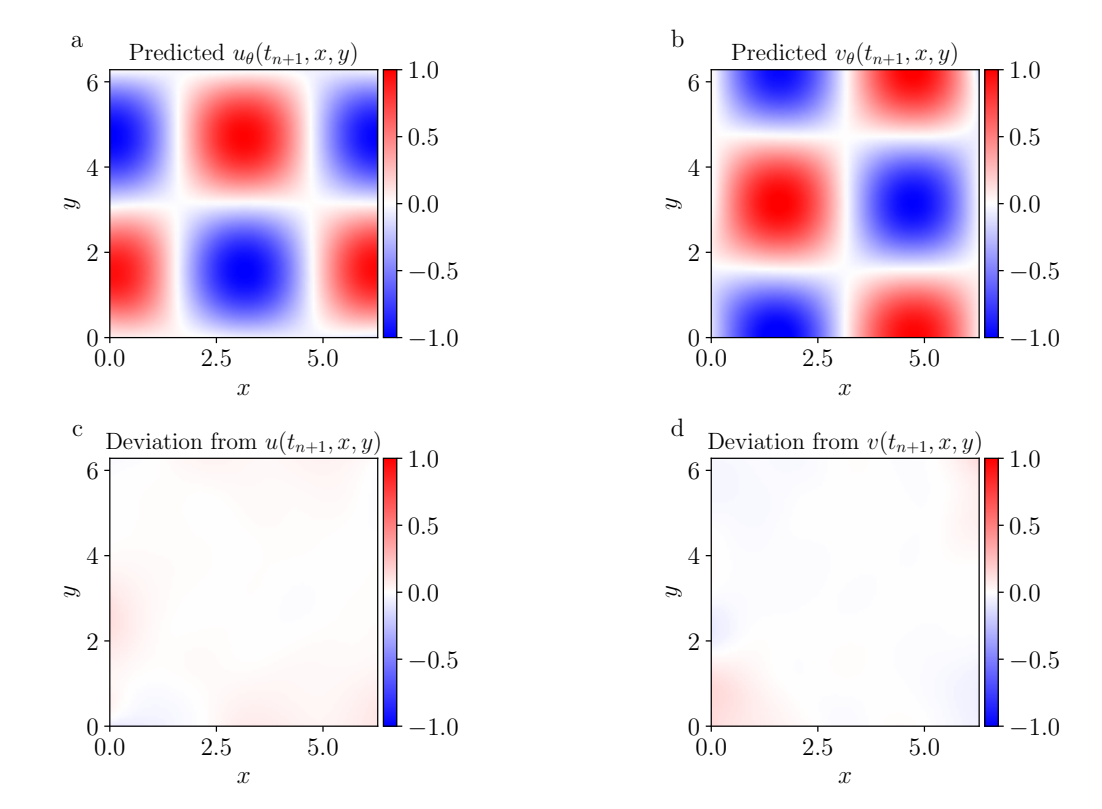


Figure 4: Fit to the Taylor-Green vortex data with $\nu=1$, $\rho=2$ using a IRK-PINN of order q=100 and time step $\Delta t=1$. The training was carried out for 20000 epochs with ADAM and 20000 epochs with L-BFGS-B, using an MLP with 10 hidden layers with 16 nodes each and SiLU activation function, and a sampling of N=300 points. (a) and (b) The results of the trained neural network prediction for $u(t_{n+1},x)$ and $v(t_{n+1},x)$, respectively. (c) and (d) Deviation from the analytical solution in (14). Total L^1 -error =2.01%

By restricting the domain of the solutions to the 2-dimensional plane $\mathbf{x} \in \Omega = [0, 2\pi]^2$, the analytical solution takes the form

$$u(t, x, y) = \sin(x)\cos(y)\exp(-2\nu t) \tag{14a}$$

$$v(t, x, y) = -\cos(x)\sin(y)\exp(-2\nu t)$$
(14b)

$$p(t, x, y) = -\frac{\rho}{4}(\cos 2x + \cos 2y) \exp(-4\nu t).$$
 (14c)

For our simulations, we fixed both the viscosity $\nu=1$ and the mass density $\rho=2$. In addition, we also fed the pressure p(t,x,y) to the PINN such that its objective is only to predict both components of the velocity fields u and v. The results of the simulation and the details of the neural networked employed are shown in FIG. 4. The IRK-PINN is able to learn the solution for a large time step with high accuracy, even when both the input and output dimensions are not one-dimensional.

D Data availability

The code and data used of all example simulations is available at https://gitlab.desy.de/CMI-public/runge-kutta-pinn.